nature physics

Article

https://doi.org/10.1038/s41567-023-02136-x

Unconventional colloidal aggregation in chiral bacterial baths

Received: 13 September 2022

Accepted: 15 June 2023

Published online: 27 July 2023

Check for updates

Daniel Grober[1,2], Ivan Palaia[1], Mehmet Can Uçar[1], Edouard Hannezo[1], Anđela Šarić[1] & Jérémie Palacci[1,2]

When in equilibrium, thermal forces agitate molecules, which then diffuse, collide and bind to form materials. However, the space of accessible structures in which micron-scale particles can be organized by thermal forces is limited, owing to the slow dynamics and metastable states. Active agents in a passive fluid generate forces and flows, forming a bath with active fluctuations. Two unanswered questions are whether those active agents can drive the assembly of passive components into unconventional states and which material properties they will exhibit. Here we show that passive, sticky beads immersed in a bath of swimming *Escherichia coli* bacteria aggregate into unconventional clusters and gels that are controlled by the activity of the bath. We observe a slow but persistent rotation of the aggregates that originates in the chirality of the *E. coli* flagella and directs aggregation into structures that are not accessible thermally. We elucidate the aggregation mechanism with a numerical model of spinning, sticky beads and reproduce quantitatively the experimental results. We show that internal activity controls the phase diagram and the structure of the aggregates. Overall, our results highlight the promising role of active baths in designing the structural and mechanical properties of materials with unconventional phases.

In the classical picture of Brownian motion, the incessant motion of microscopic particles results from collisions with the fluid molecules. The particles and solvent are passive, driven by thermal fluctuations[1,2]. Agitated molecules diffuse, interact and collide, building materials. This view of assembly constituted an elemental inspiration for colloidal science, which aims to translate the versatility of chemistry to the microscale. It led to the design of a broad library of building blocks (1–10 μm in size) with various shapes and chemical properties to mimic chemical bonds[3]. A major obstacle remains, as thermal energy is not sufficient to allow micrometric particles to explore the conformational space efficiently, making assembly challenging and often elusive[4,5]. In living systems, assembly is assisted by molecular motors that generate active fluctuations[6,7] and enhance intracellular transport[8,9]. Active agents present in a solvent generate forces and flows, adding active noise to thermal fluctuations. They constitute an effective medium, an active bath, that can, in principle, overcome kinetic barriers and control the (non-equilibrium) assembly of passive building blocks. Libchaber coined the term bacterial bath to describe the effect of swimming *Escherichia coli* on the positional fluctuations of micron-scale tracers[10], later extended to suspensions of self-propelled particles, namely nanorods or bacteria at different concentrations and speeds[11]. Active baths can be defined with an effective temperature as hot thermal systems under certain conditions[12] but remain intrinsically non-equilibrium, featuring properties prohibited by thermal physics. Active baths produce work[13], power asymmetric gears[14,15] and modulate effective interparticle interactions[16,17]. Yet, the use of active baths to control assembly has largely been unexplored.

Here, we investigate the aggregation of sticky colloids in an active bath of swimming *E. coli* bacteria. We show that the bacterial bath presents features of a hot thermal bath, effectively enhancing the dynamics of assembly. We further report that the aggregates exhibit a slow and persistent clockwise rotation, which makes the bacterial bath effectively chiral and controls the morphology and phase diagram of aggregation. Our results are quantitatively reproduced by a minimal

[1]IST Austria, Klosterneuburg, Austria. [2]Department of Physics, University of California San Diego, San Diego, CA, USA. e-mail: jeremie.palacci@ist.ac.at

https://doi.org/10.1038/s41567-023-02136-x

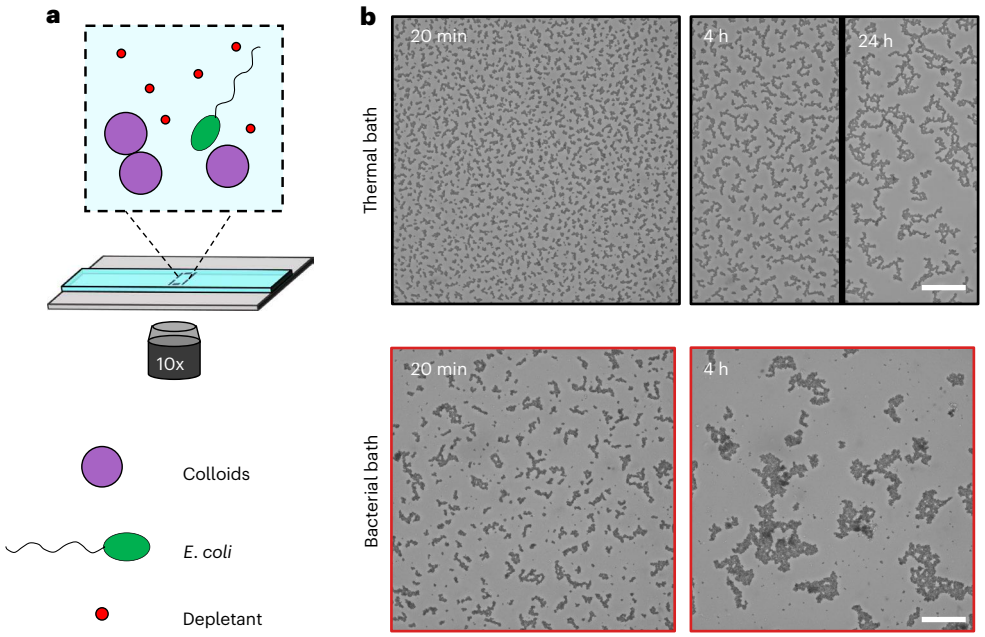

Fig. 1 | Experimental set-up and bright-field images of aggregates. a, Sketch of the experimental set-up showing the components in the aggregation of sticky beads. Colloidal beads (purple) are mixed with a depletant (red), which controls the strong attraction between the colloidal beads. The suspension is mixed with either a pure motility medium (the thermal bath) or swimming *E. coli* bacteria (green) suspended in the motility medium (the bacterial bath). **b**, Bright-field images of the colloidal aggregation after 20 mins, 4 h and 24 h in a thermal bath (top, black) and after 20 mins and 4 h in an active bath (bottom, red) with bacterial concentration $\rho_B \approx \rho^* = 6 \times 10^8$ cells per millilitre. Scale bars, 100 µm.

numerical model of attractive spinners, demonstrating the importance of the non-equilibrium rotation and folding in the reshaping of aggregates and the structuring of gels. We further highlight how the mechanical properties of such materials, assembled in active baths, differ from conventional, thermal ones.

The experiment used colloidal beads (2.2-µm 3-(trimethoxysilyl) propyl methacrylate spheres) immersed in a suspension of swimming *E. coli* bacteria. Short-range attractions between the beads were produced using a conventional depletion interaction with a non-absorbing polymer as depletant, namely poly(ethylene oxide) (PEO) with a molecular weight (MW) of 600,000 Da. We performed our experiments with an attraction strength of ~75 k_BT, where k_B is the Boltzmann constant and T is the ambient temperature, which effectively led to irreversible binding of the colloidal beads after collisions, dubbed sticky colloids (Methods). A solution of sticky colloids, that is colloidal beads and depletants ([PEO] = 3.25 g l^{-1}), was added to either a pure motility medium (the thermal bath) or swimming *E. coli* bacteria suspended in the motility medium, at concentration ρ_B (the active bath), and sealed in a glass capillary (Supplementary Information). To keep the activity of the bath constant in anaerobic conditions, we added 1% w/v glucose to the suspension, enabling the *E. coli* to swim at a constant speed, $V = 23\ \mu m\ s^{-1} \pm 2\ \mu m\ s^{-1}$ throughout the 4-h duration of an experiment (Supplementary Fig. 2)[18,19]. The concentration ρ_B of *E. coli* bacteria in the bath was controlled via optical density and adjusted by centrifugation and resuspension for each experiment (Supplementary Fig. 1). We examined active baths with various bacterial concentrations ρ_B, such that the maximal value $\rho^* = 6 \times 10^8$ cells per millilitre was an order of magnitude below the onset of bacterial turbulence[20].

The glass capillary containing the sticky beads was laid on the programmable stage of an optical microscope and observed (Fig. 1a). The particles sedimented to form a near two-dimensional (2D) system, at constant surface fraction $\Phi_S \approx 18 \pm 3\%$. Colloidal beads in the passive bath were agitated thermally. They collided and bound together, forming ramified aggregates resembling those obtained in diffusion-limited colloidal aggregation (DLCA)[4]. The system reached a near steady state in the experiments when large clusters diffused too slowly to continue growing. Similar experiments performed in the active bath of swimming *E. coli* bacteria revealed an entirely different dynamical state. The aggregates appeared more agitated and grew faster than in the thermal experiments. They were also visually distinct, being more compact than the ramified aggregates of the thermal experiment and presenting cavities (Fig. 1b and Supplementary Video 1).

We compared the dynamics of the aggregates in the thermal and active baths by tracking the aggregates. Collisions between aggregates were notably identified by abrupt changes in area and perimeter, and these led to novel aggregates. In addition to the translational dynamics of the centre of mass, we used the anisotropy of the aggregates to track their orientation and quantify their angular dynamics (Supplementary Information). Due to the complex and evolving shapes of the aggregates, a coarse-grained approach was required for meaningful comparisons. Thus, we characterized the size of the aggregates by their radius of gyration R_G, as conventionally done for fluctuating polymers (Supplementary Information). The displacements were averaged over time and isotropically in space over long trajectories (>1 min), which allowed us to characterize the dynamics of the aggregates, for both translations and rotations, by their size R_G and the concentration of the bacteria suspension ρ_B (Fig. 2).

In both the thermal and active baths, the mean squared displacement of the aggregates was linear at short times ($\Delta t < 5$ s), $\Delta R^2(\Delta t) = 4D_{eff}\Delta t$, indicative of diffusive motion with effective diffusivity D_{eff} (Fig. 2a, inset). The diffusivity in the thermal bath was lower than the Stokes–Einstein prediction for bulk diffusivity in water, a result of the increased viscosity of the motility medium with suspended depletant polymers[21] and the added hydrodynamic dissipation from the proximal glass substrate of the capillary[22]. We further observed that D_{eff} increased with bacterial concentration ρ_B, being up to eightfold larger than in the thermal bath. At fixed bacterial concentration ρ_B, the diffusivity decreased with R_G, following the Stokes–Einstein scaling for a thermal system $D_{eff} = \alpha(\rho_B)/R_G$, with $\alpha(\rho_B)$ a function of ρ_B extracted by fitting the data (Fig. 2a). Although non-monotonic behaviour of the

https://doi.org/10.1038/s41567-023-02136-x

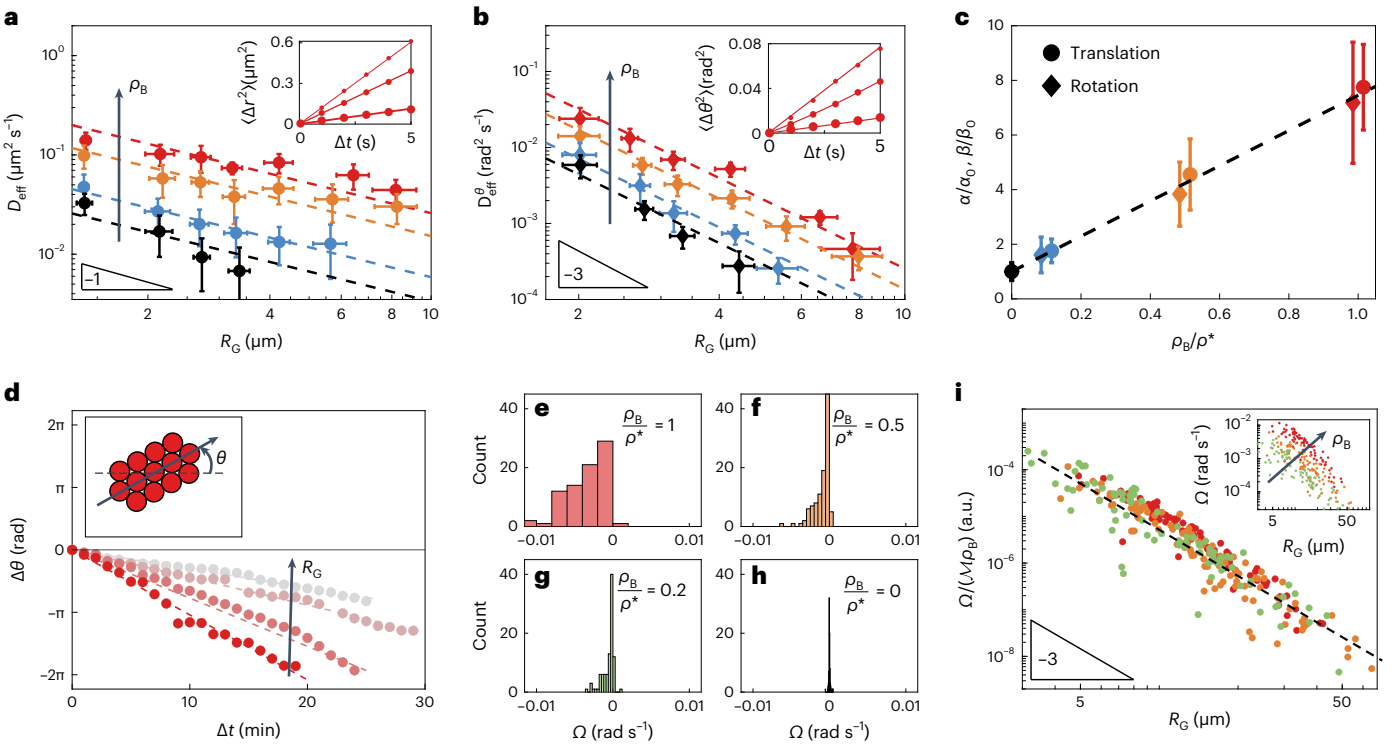

Fig. 2 | Short- and long-time dynamics of the aggregates. Short-time dynamics of the aggregates ($\Delta t < 5$ s): **a**, Inset: mean squared displacement for fixed bacterial concentration $\rho_B = \rho^*$ and increasing aggregate size R_G (larger symbols for larger R_G). The mean squared displacement increased linearly with time, with an effective diffusivity $D_{eff}(\rho_B, R_G)$. **a**, Translational diffusivity D_{eff} for various bacterial concentrations ρ_B and aggregate sizes R_G (black is thermal and hotter colours represent higher ρ_B). Dashed lines are the Stokes–Einstein predictions $D_{eff} = \alpha(\rho_B)/R_G$. Data symbols with error bars represent the average and standard deviation for more than five aggregates. **b**, Inset: mean squared angular displacement for fixed bacterial concentration $\rho_B = \rho^*$ and increasing aggregate size R_G (larger symbols for larger R_G). The mean squared angular displacement increased linearly with time, with an effective diffusivity $D^{\theta}_{eff}(\rho_B, R_G)$. **b**, Rotational diffusivity D^{θ}_{eff} for various bacterial concentrations ρ_B and aggregate sizes R_G (black is thermal and hotter colours represent higher ρ_B). Dashed lines are the Stokes–Einstein predictions $D^{\theta}_{eff} = \beta(\rho_B)/R_G^3$. Data symbols with error bars represent the average and standard deviation for more than five aggregates. **c**, Normalized diffusivity for translations α/α_0 (circles) and rotations β/β_0 (diamonds), where subscript 0 refers to the thermal bath. The normalized translational and rotational diffusivity collapsed. The symbols are slightly offset on the horizontal axis for clarity and represent the average and standard deviation (error bars). Long-time dynamics of the aggregates: **d**, Persistent clockwise rotation of aggregates observed at longer times (minutes to tens of minutes) in the glass capillary. The linear dependence of the angle θ (defined as in the inset) allowed us to extract a rotation rate $\Omega(\rho_B, R_G)$. **e**–**h**, Histograms of rotation rates Ω for different bacterial concentrations ρ_B for all aggregate sizes R_G: $\rho_B = \rho^*$ (**e**); $\rho_B = 0.5\,\rho^*$ (**f**); $\rho_B = 0.2\,\rho^*$ (**g**); $\rho_B = 0$, thermal (**h**). **i**, Inset: rotation rates Ω for different bacterial concentrations ($\rho_B \approx 0.2\,\rho^*$ (green), $\rho_B \approx 0.5\,\rho^*$ (orange) and $\rho_B \approx \rho^*$ (red), with $\rho^* = 6 \times 10^8$ cells per millilitre) and aggregate sizes R_G. **i**, Data collapsed onto the master curve $\Omega/(\mathcal{M}\rho_B) \propto 1/R_G^3$, where $\mathcal{M}$ is the mass of an aggregate particle. Each point represents a measurement of an aggregate particle.

diffusivity of spheres in a bacterial suspension has been previously reported[23], this was only studied over a narrow range of sizes and the results are compatible with our observations for aggregates of complex shapes and varying sizes. Next, we studied the orientational dynamics of the aggregates. The dynamics of the orientation θ were similarly diffusive at short times, with $\Delta\theta^2(\Delta t) = 2D^{\theta}_{eff}\Delta t$ and D^{θ}_{eff} the angular diffusivity (Fig. 2b, inset). As for translational diffusion, D^{θ}_{eff} increased with increasing bacterial concentration ρ_B and followed the Stokes–Einstein scaling: $D^{\theta}_{eff} = \beta(\rho_B)/R_G^3$, with $\beta(\rho_B)$ a function of ρ_B extracted by fitting the data (Fig. 2b).

To compare the amplitude of the fluctuations that led to the translational and rotational diffusion in the active bath, we normalized the measured diffusivities by the value in the thermal bath and plotted $\alpha(\rho_B)/\alpha_0$ and $\beta(\rho_B)/\beta_0$, where $\alpha_0 = \alpha(0)$ and $\beta_0 = \beta(0)$ refer to the thermal system (Fig. 2c). Two comments are in order: (1) The normalized fluctuations α/α_0 and β/β_0 collapsed, highlighting that the fluctuations of the active bath were the common origin of the observed translational and rotational diffusion. (2) The normalized fluctuations scaled linearly with bacterial concentration ρ_B. These results agree with previous reports of the enhanced translational diffusivity of individual spheres in an active suspension[11] and extend the conclusions to tracers with complex shapes and a broader range of sizes. The same holds for the rotational dynamics. Thus, ρ_B is a relevant experimental parameter for controlling the activity of a bacterial bath.

Our observations of the aggregates over tens of minutes revealed a small but persistent angular rotation, $\Omega < 10^{-2}$ rad s^{-1}, which was previously imperceptible at shorter times (Fig. 2d and Supplementary Video 2). The rotation was consistently clockwise in experiments performed in the capillary (Fig. 2e–h), at a rate that increased with the bacterial concentration ρ_B and decreased with aggregate radius R_G (Fig. 2i, inset). Remarkably, the data collapsed onto a master curve, $\Omega/(\mathcal{M}\rho_B) \propto 1/R_G^3$, where $\mathcal{M}$ is the mass of an aggregate particle (Fig. 2i). This indicates that a net torque $\tau \propto \mathcal{M}\rho_B$ was imparted from the active bath to the aggregates and balanced by a viscous torque proportional to $1/R_G^3$. This linear dependence of the torque on the bacterial concentration ρ_B demonstrates the cumulative effect of the bacteria bath and led to the rotation of the aggregates in a persistent (clockwise) direction. It notably departs from the non-chiral rotation that arises from the summation of random contributions from bacteria in an aggregate[24]. By extracting the mobility μ_R from the measurements of rotational diffusivity in the thermal bath (Fig. 2b), we estimated the net torque exerted by the bacterial bath, $\tau_{R_G} = \mu_R^{-1}\Omega(R_G) \approx 0.4$pN μm for $R_G \approx 7$ μm.

https://doi.org/10.1038/s41567-023-02136-x

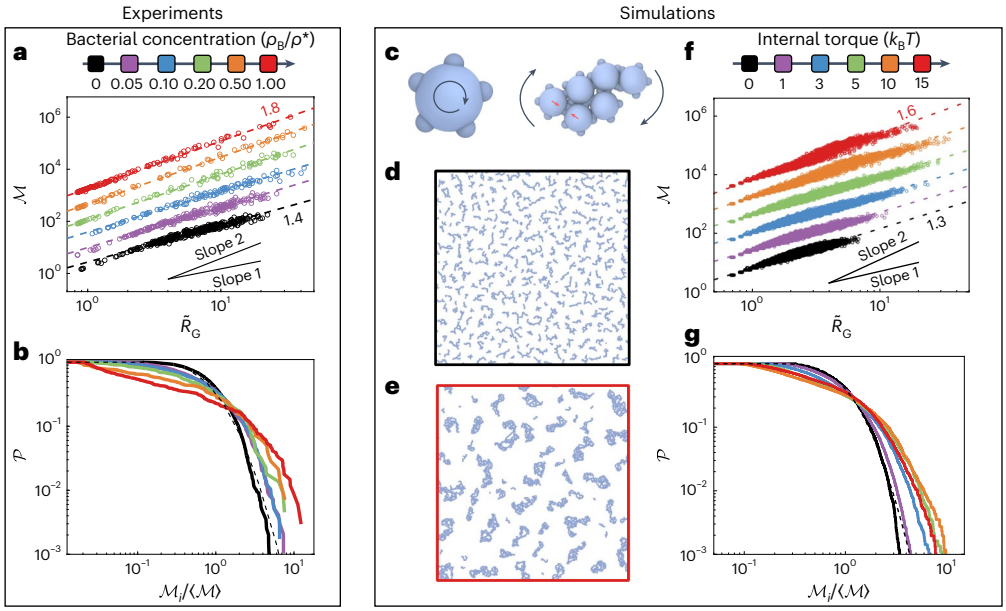

Fig. 3 | Aggregate morphology and size distributions. Experiments: **a**, Measurements of the fractal dimension ν, as $\mathcal{M} \propto \tilde{R}_G^{\nu}$ for aggregates with radii $\tilde{R}_G = R_G/a$, where a is the radius of a colloidal bead and $\mathcal{M}$ is mass. **b**, Complementary cumulative size distributions $\mathcal{P}$ of the aggregates with increasing bacterial concentration ρ_B (black is thermal, ranging from 0.05 ρ^* to ρ^*; see colour bar). The black dashed line is the log-normal distribution predicted for passive colloidal aggregation. In both **a** and **b**, the aggregates were characterized after 4 h. Simulations: **c**, Sketch of a computational model of active spinners with internal torque and attractive interactions coupled by tangential friction (Supplementary Information and Supplementary Fig. 13). **d**–**e**, Snapshots of the simulations of our minimal model for thermal (black) (**d**) and active (**e**) baths with an internal torque (red). See the main text. The results resemble the experimental results in Fig. 1b. **f**, Measurements of the fractal dimension $\mathcal{M} = R_G^{\nu}$ of aggregates in the simulations. **g**, Complementary cumulative size distributions $\mathcal{P}$ of the aggregates with increasing internal torque; see colour bar. The black dashed line is the log-normal distribution predicted for passive colloidal aggregation.

This minute torque became noticeable in aggregation experiments lasting a few hours. We intuit that the rotational symmetry-breaking originates from the native chirality of *E. coli* flagella, which resulted in clockwise circular trajectories with typical radius of curvature $R_B \approx 43$ μm (Supplementary Fig. 3) near the no-slip boundary of the glass capillary[25]. Indeed, we could reverse the direction of rotation of the aggregates by performing experiments at the air–water interface of a pendant drop, where the direction of rotation of the bacteria reverse so that they move in counterclockwise circles[26] (Supplementary Fig. 4). This confirms that the chirality of *E. coli* flagella breaks the rotational symmetry and makes the bacterial bath effectively chiral.

To understand the phenomenon better, we considered a toy model of a circular aggregate of radius a in an active bath of persistent self-propelled rods. For simplicity, the self-propelled particles exert a constant force $\mathbf{F}_0$ aligned with their propulsion direction (Supplementary Information and Supplementary Fig. 5). When the self-propelled particles navigate along straight segments, no net torque is exerted due to symmetry and the circular aggregate does not show persistent rotation[14,15]. In contrast, when the self-propelled particles move along circular clockwise trajectories, a wedge of unbalanced collisions appears. Its opening angle 2θ is controlled by the curvature $1/R_B$ of the trajectories, $\theta \approx 1/R_B$ (Supplementary Fig. 5). The asymmetric collisions lead to a tangential force of amplitude $F_{//} \propto 2\theta \times F_0$, which exerts a torque on the circular aggregate. The total torque, $\tau_{R_B} \propto (F_0/R_B)\rho_B a^2$, is obtained by integration over the perimeter and multiple collisions and leads to clockwise rotation of the circular aggregate. Thus, this simple toy model highlights that an active chiral bath exerts an active torque on a circular aggregate, which is absent for an active bath of straight swimmers. We further extend this result, showing that an active bath that results in constant tangential forces along the boundary of an aggregate produces a torque proportional to $\rho\mathcal{A}$, that is, proportional to the surface area $\mathcal{A}$ of the aggregate (Supplementary Information).

Remarkably, this scaling, valid for aggregates of arbitrary shapes, agrees with the experimental results (Fig. 2i). We do, however, stress that, quantitatively, the rotation of the aggregates in the experiment is certainly more complicated than in this simple model, as the rotation is due to a superimposition of the effects of the complex shape of the aggregates, which can be locally asymmetric, as well as the forces exerted by the bacteria navigating inside the aggregate, as visible in Supplementary Fig. 3c. A quantitative description of these effects lies beyond the scope of this paper and constitutes further work.

Next, we considered the morphology and statistical properties of the colloidal aggregates formed in the thermal and active baths. To account for the accelerated dynamics of the active bath, we rescaled time so that the aggregates in the thermal and active baths reached the same average size. Aggregates formed after 25 h (thermal bath) or 1.25 h (active bath) reached comparable sizes, $\mathcal{M} = 150$ colloids, but were different to the naked eye (Supplementary Fig. 6). The thermal aggregates were ramified, as is typical of DLCA, due to the low probability that a diffusing particle would reach the centre of the aggregate. In contrast, the aggregates in the active bath were compact and had cavities. Remarkably, aggregates that formed in either the thermal or active baths fall into distinct groups based on the fraction of colloids at the perimeter, a salient control parameter in the mechanical response of gels[27] (Supplementary Fig. 8). To quantify the morphological changes further, we computed the fractal dimensions ν of an ensemble of aggregates, as $\mathcal{M}_i \propto R_{G,i}^{\nu}$, where $\mathcal{M}_i$ is the mass, or number of colloids, in aggregate i and $R_{G,i}$ is the radius of gyration of aggregate i (Fig. 3a). Aggregates for which $\nu = 1$ are elongated, whereas those with $\nu = 2$ are compact. Intermediate values of ν are indicative of ramified, fractal structures. The fractal dimensions of the aggregates in the thermal bath and the active bath evolve in time before reaching a plateau after approximately 2 h (Supplementary Fig. 9). The value of the fractal dimension measured in the thermal bath, $\nu_0 \approx 1.4$, agrees with values

https://doi.org/10.1038/s41567-023-02136-x

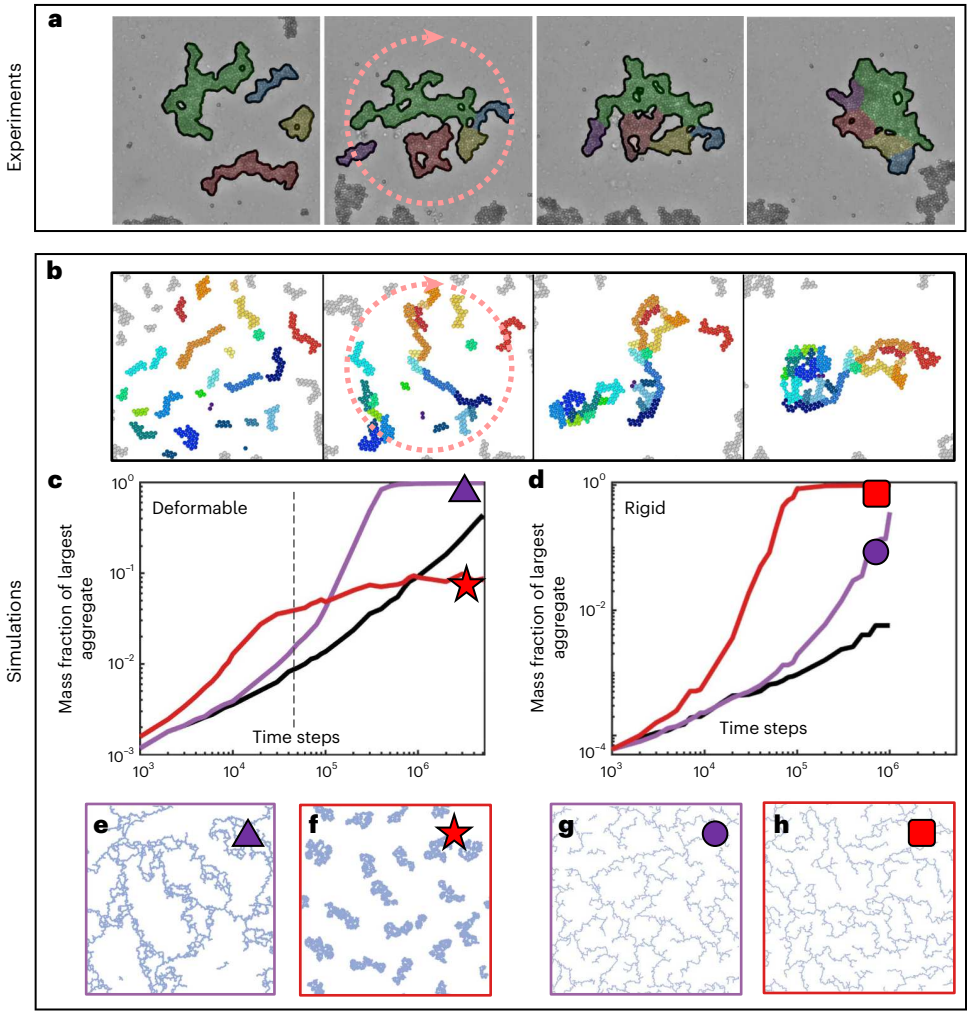

Fig. 4 | Rotation and folding of aggregates. a,**b**, Rotation and folding of aggregates in experiments (**a**) and simulations (**b**) leading to the compaction of the aggregates in an active bath. Red arrows indicate the direction of rotation of the aggregates. **c**–**h**, Simulations. Colours indicate the internal torque: 0 k_BT (black), 1 k_BT (purple) and 15 k_BT (red). **c**,**e**,**f**, Simulations of deformable aggregates (see main text) **c**, Time evolution of the mass fraction of the largest aggregate in the system for spinners with different internal torques. The mass fraction is the fraction of colloids in the largest aggregate with respect to the total number of colloids. The rotation of the aggregates accelerates growth in comparison with thermal aggregation (black line). In the thermal case and at low activity, the largest aggregate grows until it incorporates all the particles to form a percolated structure and a space-spanning network, as visible in the snapshot of the simulation (**e**), corresponding to the purple triangle in **c**. With sufficient activity (red curve), large aggregates fold and the largest cluster becomes more compact, exhibiting a plateau of growth (after the vertical dashed line). The gel phase is suppressed and replaced by compact clusters with cavities, as visible in the snapshot of the simulation (**f**), corresponding to the red star in **c**. **d**,**g**,**h**, Simulations of rigid aggregates (see main text). **d**, Time evolution of the mass fraction of the largest aggregate in simulations of rotating rigid aggregates, without folding. **g**,**h**, Snapshots of the simulations as indicated by the symbols in **d**. The formation of a percolated structure is shown for all levels of activity (internal torque). The folding suppresses the gel phase at higher activity levels.

reported for DLCA in 2D[28]. As observed by the naked eye, aggregates in the active bath were more compact than those in the thermal bath, reaching $\nu(\rho^*) \approx 1.8$ for the highest activity level.

The aggregate morphology was further quantified via the normalized complementary cumulative size distribution $\mathcal{P}$, corresponding to the probability for an aggregate to be larger than a given size (Supplementary Information). In the thermal bath, the size distribution of aggregates can be rescaled by the mean value, such that at all times the distributions collapse onto a single log-normal distribution (Supplementary Fig. 10), a universal feature of merging and fragmenting systems[29,30]. In contrast, the size distribution of aggregates formed in the active baths cannot be collapsed and exhibits significant deviations from log-normal. Notably, the tails become more prominent with increasing activity (Fig. 3b). Thus, aggregation in the thermal and active baths do not belong to the same universality class, highlighting a profound effect of the bacterial bath on the aggregation properties[29,30]. We intuit that those non-equilibrium properties originate in the compaction and folding of the aggregates, which are due to the observed rotation (Fig. 4a).

To understand the mechanism better, we developed a minimal physical model that aims to capture the chirality of the bacterial bath without explicitly considering the swimming bacteria. We expected the chiral bath to cause the aggregates of colloids to rotate, and we modelled the system as an ensemble of attractive rotating beads coupled to each other by friction (Fig. 3c and Supplementary Information). Rotation was implemented in a mean field fashion by attributing a constant torque to each bead. These molecular dynamics simulations were similar in spirit to previous models of internally driven gears[31,32] with the addition of strong attraction between the spinners. The latter leads to irreversible aggregation, a notable difference from crystals of rotating cells reported at moderate attraction[33]. The clockwise rotation of the beads was implemented via an internal driving torque whose amplitude controls the internal activity of the system, thus allowing comparisons between the simulations and our experimental results. The

https://doi.org/10.1038/s41567-023-02136-x

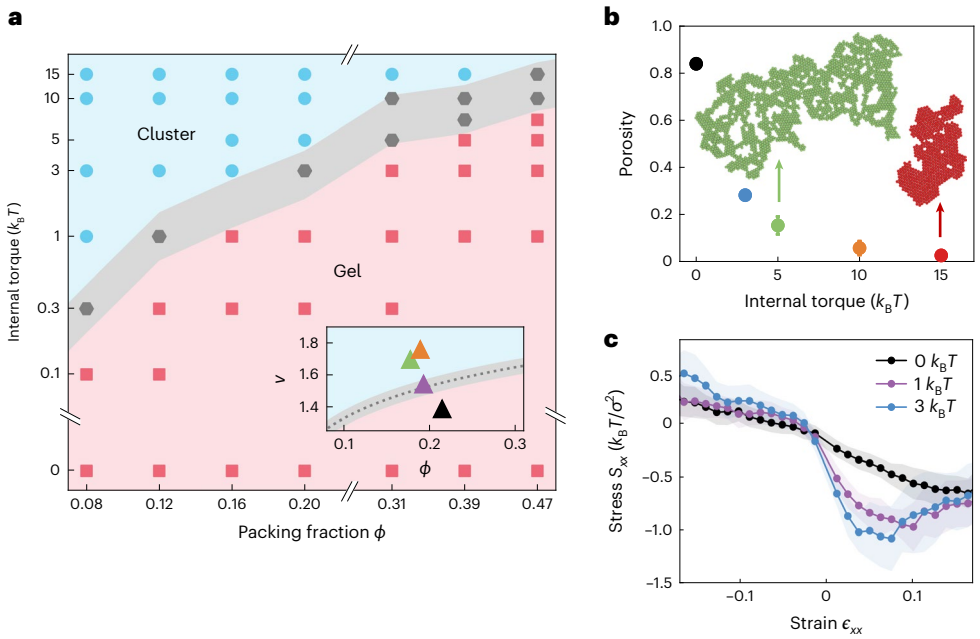

Fig. 5 | Activity controls phases, structures and mechanics of aggregates. **a**, Phase diagram of colloidal aggregation for various internal torques and surface fractions showing the existence of a space-spanning gel phase (pink) and cluster phase (blue) controlled by the activity. Squares and circles are simulated data. Inset: phase diagram in the (ν,Φ) plane obtained by measuring the fractal dimension of the aggregates. The gel phase (pink) is separated from the cluster phase (blue) by a critical fractal dimension $\nu_C \approx 2 + 0.29 \log \Phi$ (dashed line). See the main text for the scaling. Triangles are experimental data for different levels of activity: thermal (black), $\rho_B = 0.05\,\rho^*$ (purple), $\rho_B = 0.2\,\rho^*$ (green) and $\rho_B = 0.5\,\rho^*$ (orange). **b**, Activity control of the structure of aggregates. Simulations performed at constant $\Phi = 0.16$. The system is in a gel phase in the thermal bath (black circle) and, for all other represented activities, forms compact clusters (shown as insets), whose porosity is set by the internal torque. Data symbols with error bars display the average and standard deviation over 16 realizations of the simulation. **c**, Mechanical stress versus strain curves of passive gels whose initial structures were prepared through thermal (black) or active aggregation based on the amplitude of the internal torque, as indicated by the colour of the curve: 1 k_BT (purple) and 3 k_BT (blue). All simulations were performed with initial structures prepared at $\Phi = 0.31$. The extensile response (positive strain) is markedly different for gels obtained via thermal or active aggregation. The gels assembled in the thermal bath responded linearly and symmetrically, behaving as an elastic solid in the range shown. The gels produced through active aggregation were highly nonlinear, elastic in compression and stiff under extension. Compression and extension curves are plotted independently (see Supplementary Information for the deformation protocol). Each data symbol is the average of 24 measurements and the error bars show the standard deviation (Supplementary Information).

numerical simulations capture visually the difference between aggregation in the thermal and active baths (Fig. 3d,e and Supplementary Videos 3–5). They, furthermore, reproduce quantitatively the experimental increase in fractal dimensions and the size distributions of the aggregates (Fig. 3f,g), thus validating the predictive power of the model. The aggregates rotated and grew faster than with thermal aggregation, in line with a simple analytical model of aggregation and collision that accounts for the sweeping effect of the rotation on the collision rate (Supplementary Fig. 11). The simulations, like the experiment, show two different effects of the rotation: (1) the mentioned sweeping motion of spinning aggregates and (2) the self-folding of the aggregates (Fig. 4b and Supplementary Video 6).

To disentangle their role, we compared our initial set of simulations, where aggregates can deform as a result of their internal torques (Fig. 4c), with another set where the aggregates were treated as rigid objects (Fig. 4d). At low internal torque, the simulations of both deformable and rigid aggregates formed 2D gels (Fig. 4c,d). The structures obtained were, however, markedly different. The gels formed by the percolation of deformable aggregates were structurally heterogeneous, with both compact and ramified regions (Fig. 4e). The gels built from rigid aggregates appeared more uniform in structure (Fig. 4g). At sufficient internal torque, the simulations of rigid aggregates produced space-spanning networks that resemble thermal DLCA gels (Fig. 4g,h). In contrast, the deformable aggregates do not percolate at high internal torques, as the internal torque folds each large, deformable aggregate onto itself. This leads to large compact clusters with internal cavities (Fig. 4f) and prevents the formation of a percolated network (Fig. 4c). The rotation enhances the dynamics of aggregation while the self-folding of the ramified aggregates controls their fractal dimension. This mechanism highlights the difference in the nature of the reported aggregation with conventional reaction-limited colloidal aggregation and leads to different morphologies[4].

We next investigated the phase behaviour of aggregation for various surface fractions Φ and internal torques. We observed a gel phase and a cluster phase controlled by the activity (Fig. 5a). The (ν,Φ) plane was obtained by measuring the fractal dimension of the aggregates, which allowed us to characterize the experimental data in the bacterial baths (Fig. 5a inset and Supplementary Fig. 12). The gel phase was separated from the cluster phase by a critical fractal dimension $\nu_C \approx d + \alpha \log \Phi$, where $d = 2$ is the dimension of space and $\alpha \approx 0.29$ is phenomenologically adjusted to the data, the scaling in $\log \Phi$ originating from the definition of $\Phi \propto \mathcal{M}$ (ref. 5). Overall, sufficient activity suppressed the gel phase in favour of compact aggregates.

Having established that the activity of the bath controls the phase behaviour of aggregation into a cluster phase or a gel phase, we next investigated the structural and mechanical properties of each phase. We observed for the cluster phase that the porosity of aggregates is controlled by the internal activity. Increasing the internal torque augments the compaction of the aggregates, leading to dense and compact structures (Fig. 5b). We considered 2D gels (at $\Phi = 0.31$) assembled in a thermal bath or with internal activity. We probed those passive gels mechanically by numerically measuring the stress and strain

https://doi.org/10.1038/s41567-023-02136-x

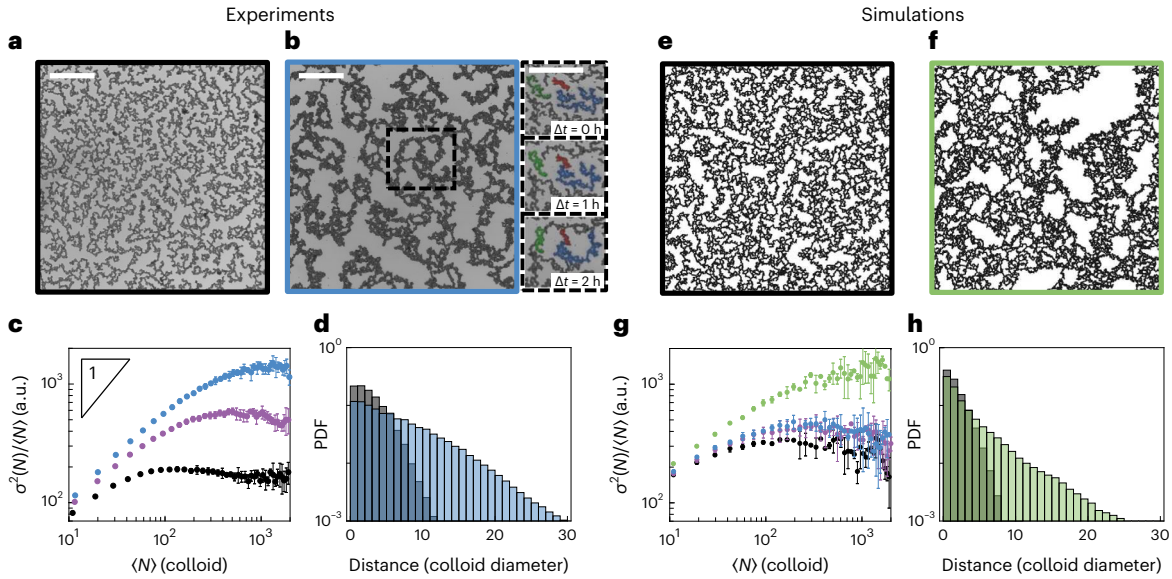

Fig. 6 | Structure of gels in passive and active baths. a–d, Experimental results. Bright-field images of a 2D colloidal gel aggregated in a thermal bath ($\rho_B = 0$) (**a**) and an active bath ($\rho_B = 0.1\,\rho^*$) (**b**). Scale bars, 200 µm. **b**, Inset: time-lapse micrographs showing the formation of large heterogeneities via the rotation and jamming of large aggregates. Scale bar, 200 µm. **c**, Number fluctuations $\sigma^2(N)/\langle N\rangle$ of colloidal gels aggregated in a thermal bath and an active bath for various strengths (Supplementary Information). The average and standard deviation were calculated for five realizations of the experiment. **d**, Probability density function (PDF) of the distance from the colloidal backbone to points of the pores. Grey represents the thermal bath ($\rho_B = 0$) and blue the active bath ($\rho_B = 0.1\,\rho^*$). **e–h**, Simulation results. Snapshots of simulated 2D colloidal gels, aggregated with an internal torque of 0 k_BT (**e**) or 5 k_BT (**f**). **g**, Number fluctuations $\sigma^2(N)/\langle N\rangle$, calculated from simulated colloidal gels. Average and standard deviation are calculated for all data subsets obtained from space tiling, for two realizations of the simulation (Supplementary Information). **h**, PDF of distance to the nearest colloid for all pixels in holes in the simulated colloidal gels. Grey represents a gel aggregated at an internal torque of 0 k_BT and green at 5 k_BT. Again, there is good agreement between the simulation results and the experimental results.

(Supplementary Videos 7 and 8). Gels obtained by aggregation in the thermal bath exhibit conventional elastic behaviour in the limited range of the strain considered, namely ~10%. By contrast, gels assembled due to internal activity were highly nonlinear and behaved like mechanical diodes: elastic in compression and stiff under extension (Fig. 5c). The onset of the plastic regime also appeared to be controlled by the activity of the assembly.

To gain insights into the origin of this unconventional mechanical behaviour, we performed additional experiments and simulations, at $\Phi = 0.39$, a surface fraction for which we can experimentally achieve a 2D percolated network greater than 1 mm × 1 mm in size in both the thermal and bacterial baths. We used bacterial concentrations of up to $\rho_B = 0.1\,\rho^*$, beyond which the gel phase is replaced by the cluster phase. Once again, there was good agreement between our experiments and the phase diagram predicted numerically (Fig. 5a). The gels produced in the active baths had significant structural differences compared to those achieved thermally (Fig. 6a,b). This could be seen as surprising, considering that the added fluctuations of the bacterial bath were comparable to the thermal energy itself (Fig. 2c). It simply highlights that the bacterial bath is more than a mere hot bath and that the acquired rotation of the aggregates has a profound effect on the dynamics and structure of the aggregates, as already apparent from the anomalous size distributions (Fig. 3b,g).

We quantified the structural differences by measuring the density fluctuations of the gels (Fig. 6c). We can define a typical length scale for the gel structure by identifying the local maximum of the number fluctuations $\sigma^2(N)/\langle N\rangle$ (ref. 34). As visible to the naked eye, the length scale grows from ~10 colloid diameters in the thermal gel to ~30–40 colloid diameters in the gels assembled in the bacterial bath. Additionally, the emergence of giant number fluctuations for gels assembled in the active bath highlight that the structures were more heterogeneous compared to those in the passive bath. To further quantify this aspect, we characterized the pores of the 2D gels by computing the distance from points in a pore to the nearest colloid in the network backbone[35], as plotted in Fig. 6d. Gels assembled in the active baths had broader distributions than gels assembled thermally, indicative of large heterogeneous voids in the structure. These structural heterogeneities arise from the rotation of the aggregates induced by the chiral bacterial bath. The rotation results in the ramified aggregates jamming into each other and the formation of large isostatic structures (Fig. 6b, inset). Remarkably, the results from our simple numerical model of rotating aggregates with internal torques is again in good agreement with the results from our experimental realization of gels (Fig. 6g,h). This highlights how rotation and folding of the aggregates are the key ingredients in shaping and forming heterogeneous structures and driving exotic mechanical responses, in line with the role of structural heterogeneities in determining the breaking and restructuring of gels[36,37].

Previous works reported that the moderate substitution of passive particles by active particles facilitates the annealing of colloidal monolayers[38,39] or can control the yield stress of gels[40,41]. Our results highlight how the assembly in an active bath directs the structural and mechanical properties of materials entirely made of passive constituents. We are hopeful that our results will stimulate future work and lead to a complete microscopic model that translates aggregation in bacterial baths into the design of gels with unconventional mechanical responses.

In summary, we have demonstrated that active baths are a potent instrument for producing unconventional aggregates and gels and that activity is a salient parameter for phases of matter out of equilibrium. It is noticeable that simulations of a purely active system of spinners quantitatively reproduced experimental results of passive particles in a chiral bacterial bath, possibly highlighting generic features between these two classes of systems. The importance of chirality in

morphogenesis[42–44] further hints at the potential of chiral active baths to produce materials beyond what can be achieved thermally. Although our study was limited to 2D, it is a proof of concept for materials powered from within, in phases and structures not achieved via thermal treatments, as also recently highlighted for the effect of activity on liquid interfaces[45]. It will motivate efforts to assemble 3D materials in active baths, whereas the characterization of their non-conventional mechanical and rheological properties will drive further experimental and theoretical work. This work effectively lays out a road map for establishing the concept of bacterial forging, in which gels structures are controlled by the bacterial bath, the way forging in metallurgy controls the properties of metals through sequences of annealing and quenching. Because activity can, in principle, be controlled in time and space externally[46], our findings open up a branch of materials science in which the properties of passive materials are tailored during their assembly in active baths and active materials are supplied with energy as desired, to induce healing or annealing.

Online content

All methods, additional references, Nature Portfolio reporting summaries, source data, extended data, supplementary information, acknowledgements, peer review information; details of author contributions and competing interests; and statements of data and code availability are available at https://doi.org/10.1038/s41567-023-02136-x.

References

1. Perrin, J. Mouvement brownien et réalité moléculaire. *Radium* **6**, 353–360 (1909).
2. Einstein, A. The motion of elements suspended in static liquids as claimed in the molecular kinetic theory of heat. *Ann. Phys.* **17**, 549–560 (1905).
3. Hueckel, T., Hocky, G. M. & Sacanna, S. Total synthesis of colloidal matter. *Nat. Rev. Mater.* **6**, 1053–1069 (2021).
4. Lu, P. J. & Weitz, D. A. Colloidal particles: crystals, glasses, and gels. *Annu. Rev. Condens. Matter Phys.* **4**, 217–233 (2013).
5. Del Gado, E. et al. in *Fluids, Colloids and Soft Materials: An Introduction to Soft Matter Physics* (eds Fernandez-Nieves, A. & Puertas, A. M.) Ch. 14 (Wiley, 2016).
6. Brugues, J. & Needleman, D. Physical basis of spindle self-organization. *Proc. Natl Acad. Sci. USA* **111**, 18496–18500 (2014).
7. Wittmann, T., Hyman, A. & Desai, A. The spindle: a dynamic assembly of microtubules and motors. *Nat. Cell Biol.* **3**, E28–E34 (2001).
8. Brangwynne, C. P., Koenderink, G. H., MacKintosh, F. C. & Weitz, D. A. Cytoplasmic diffusion: molecular motors mix it up. *J. Cell Biol.* **183**, 583–587 (2008).
9. Guo, M. et al. Probing the stochastic, motor-driven properties of the cytoplasm using force spectrum microscopy. *Cell* **158**, 822–832 (2014).
10. Wu, X.-L. & Libchaber, A. Particle diffusion in a quasi-two-dimensional bacterial bath. *Phys. Rev. Lett.* **84**, 3017–3020 (2000).
11. Mino, G. et al. Enhanced diffusion due to active swimmers at a solid surface. *Phys. Rev. Lett.* **106**, 048102 (2010).
12. Berthier, L. & Kurchan, J. Non-equilibrium glass transitions in driven and active matter. *Nat. Phys.* **9**, 310–314 (2013).
13. Pietzonka, P., Fodor, E., Lohrmann, C., Cates, M. E. & Seifert, U. Autonomous engines driven by active matter: energetics and design principles. *Phys. Rev. X* **9**, 041032 (2019).
14. Di Leonardo, R. et al. Bacterial ratchet motors. *Proc. Natl Acad. Sci. USA* **107**, 9541–9545 (2010).
15. Sokolov, A., Apodaca, M. M., Grzybowski, B. A. & Aranson, I. S. Swimming bacteria power microscopic gears. *Proc. Natl Acad. Sci. USA* **107**, 969–974 (2010).
16. Angelani, L., Maggi, C., Bernardini, M. L., Rizzo, A. & Di Leonardo, R. Effective interactions between colloidal particles suspended in a bath of swimming cells. *Phys. Rev. Lett.* **107**, 138302 (2011).
17. Ray, D., Reichhardt, C. & Reichhardt, C. J. O. Casimir effect in active matter systems. *Phys. Rev. E* **90**, 013019 (2014).
18. Cerbino, R. & Trappe, V. Differential dynamic microscopy: probing wave vector dependent dynamics with a microscope. *Phys. Rev. Lett.* **100**, 188102 (2008).
19. Wilson, L. G. et al. Differential dynamic microscopy of bacterial motility. *Phys. Rev. Lett.* **106**, 018101 (2011).
20. Peng, Y., Liu, Z. & Cheng, X. Imaging the emergence of bacterial turbulence: phase diagram and transition kinetics. *Sci. Adv.* **7**, eabd1240 (2021).
21. Ebagninin, K. W., Benchabane, A. & Bekkour, K. Rheological characterization of poly(ethylene oxide) solutions of different molecular weights. *J. Colloid Interface Sci.* **336**, 360–367 (2009).
22. Faxen, H. Der Widerstand gegen die Bewegung einer starren Kugel in einer zahen Flussigkeit, die zwischen zwei parallelen ebenen Wanden eingeschlossen ist. *Ann. Phys.* **373**, 89–119 (1922).
23. Patteson, A. E., Gopinath, A., Purohit, P. K. & Arratia, P. E. Particle diffusion in active fluids is non-monotonic in size. *Soft Matter* **12**, 2365–2372 (2016).
24. Schwarz-Linek, J. et al. Phase separation and rotor self-assembly in active particle suspensions. *Proc. Natl Acad. Sci. USA* **109**, 4052–4057 (2012).
25. Lauga, E., DiLuzio, W. R., Whitesides, G. M. & Stone, H. A. Swimming in circles: motion of bacteria near solid boundaries. *Biophys. J.* **90**, 400–412 (2006).
26. Di Leonardo, R., Dell'Arciprete, D., Angelani, L. & Iebba, V. Swimming with an image. *Phys. Rev. Lett.* **106**, 038101 (2011).
27. Tsurusawa, H., Arai, S. & Tanaka, H. A unique route of colloidal phase separation yields stress-free gels. *Sci. Adv.* **6**, eabb8107 (2020).
28. Cerdà, J. J., Sintes, T., Sorensen, C. M. & Chakrabarti, A. Kinetics of phase transformations in depletion-driven colloids. *Phys. Rev. E* **70**, 011405 (2004).
29. Friedlander, S. & Wang, C. The self-preserving particle size distribution for coagulation by Brownian motion. *J. Colloid Interface Sci.* **22**, 126–132 (1966).
30. Rulands, S. et al. Universality of clone dynamics during tissue development. *Nat. Phys.* **14**, 469–474 (2018).
31. Spellings, M. et al. Shape control and compartmentalization in active colloidal cells. *Proc. Natl Acad. Sci. USA* **112**, E4642–E4650 (2015).
32. Nguyen, N. H. P., Klotsa, D., Engel, M. & Glotzer, S. C. Emergent collective phenomena in a mixture of hard shapes through active rotation. *Phys. Rev. Lett.* **112**, 075701 (2014).
33. Petroff, A. P., Wu, X.-L. & Libchaber, A. Fast-moving bacteria self-organize into active two-dimensional crystals of rotating cells. *Phys. Rev. Lett.* **114**, 158102 (2015).
34. Dibble, C. J., Kogan, M. & Solomon, M. J. Structure and dynamics of colloidal depletion gels: coincidence of transitions and heterogeneity. *Phys. Rev. E* **74**, 041403 (2006).
35. Torquato, S. & Avellaneda, M. Diffusion and reaction in heterogeneous media: pore size distribution, relaxation times, and mean survival time. *J. Chem. Phys.* **95**, 6477–6489 (1991).
36. Rocklin, D. Z., Hsiao, L., Szakasits, M., Solomon, M. J. & Mao, X. Elasticity of colloidal gels: structural heterogeneity, floppy modes, and rigidity. *Soft Matter* **17**, 6929–6934 (2021).
37. Colombo, J., Widmer-Cooper, A. & Del Gado, E. Microscopic picture of cooperative processes in restructuring gel networks. *Phys. Rev. Lett.* **110**, 198301 (2013).

38. Ramananarivo, S., Ducrot, E. & Palacci, J. Activity-controlled annealing of colloidal monolayers. *Nat. Commun.* **10**, 3380 (2019).
39. van der Meer, B., Filion, L. & Dijkstra, M. Fabricating large two-dimensional single colloidal crystals by doping with active particles. *Soft Matter* **12**, 3406–3411 (2016).
40. Saud, K. T., Ganesan, M. & Solomon, M. J. Yield stress behavior of colloidal gels with embedded active particles. *J. Rheol.* **65**, 225–239 (2021).
41. Omar, A. K., Wu, Y., Wang, Z.-G. & Brady, J. F. Swimming to stability: structural and dynamical control via active doping. *ACS Nano* **13**, 560–572 (2018).
42. Taniguchi, K. et al. Chirality in planar cell shape contributes to left-right asymmetric epithelial morphogenesis. *Science* **333**, 339–341 (2011).
43. Hozumi, S. et al. An unconventional myosin in *Drosophila* reverses the default handedness in visceral organs. *Nature* **440**, 798–802 (2006).
44. Tan, T. H. et al. Odd dynamics of living chiral crystals. *Nature* **607**, 287–293 (2022).
45. Adkins, R. et al. Dynamics of active liquid interfaces. *Science* **377**, 768–772 (2022).
46. Arlt, J., Martinez, V. A., Dawson, A., Pilizota, T. & Poon, W. C. K. Painting with light-powered bacteria. *Nat. Commun.* **9**, 768 (2018).

Methods

Stock solutions

For all stock solutions, chemicals were dissolved in deionized (DI) water with a resistivity of 18 MΩ cm from a Milli-Q EQ 7000 water purification system. A stock solution of 200 mM NaCl (Sigma-Aldrich, MW 58.4) was prepared by dissolving 0.12 g of NaCl in 10 ml of DI water. A stock solution of 2% w/v F108 (Sigma-Aldrich Synperonic F108 surfactant, MW 14,600) was prepared by dissolving 0.2 g of F108 in 10 ml of DI water. A stock solution of 25 g l^{-1} PEO (Sigma-Aldrich, MW 600k) was prepared by dissolving 0.25 g of PEO in 10 ml of DI water, and stirred overnight using a magnetic stirring rod until dissolved. A stock solution of 0.1 M potassium phosphate buffer, used to prepare the motility medium, was prepared by dissolving 9.34 g of K_2HPO_4 (Sigma-Aldrich, MW 174.2) and 6.31 g of KH_2PO_4 (Sigma-Aldrich, MW 136.1) in 1 l of DI water. Then, 0.5 M of ethylenediaminetetraacetic acid (EDTA) stock solution was prepared by dissolving 186.10 g of EDTA dihydrate (Sigma-Aldrich, MW 372.2) into 1 l of DI water. The pH was adjusted to 8 using NaOH pellets, to dissolve the EDTA.

Depletion interaction

We controlled the attraction between colloids using depletion interactions with PEO polymer as the depletant. Unless otherwise stated, in each experiment, we added a stock solution of PEO to a concentration of 3.25 g l^{-1}. Following the derivation given in ref. 47, we estimated the strength of the induced attraction using the following equation:

$$\frac{\Delta E}{k_B T} = -2\pi n_{dep} r^2 R\left(1 - \frac{h}{2r}\right)^2$$

where r is the radius of the depletant (57 nm), n_{dep} is the number density of the depletant, R is the radius of the colloids (1.1 µm) and h is the distance between the colloids. Setting $h = 0$, we estimated the maximum strength of the attraction to be $\Delta E = -75\, k_B T$. Additionally, we understand the strength of the attraction to be linearly proportional to the concentration of the depletant, with an interaction range proportional to the radius of the depletant.

Microscopy

All data were captured with a Nikon TI Eclipse microscope equipped a motorized stage, controlled using the Micro-Manager software. The microscope had two cameras. A Hamamatsu Orca Flash 4.0 CMOS, using a 2,048 × 2,048 pixel field of view and 16 bits, was used for taking time-lapse photographs with a frame rate of 1 frame per minute. For videos requiring a faster frame rate, we used an Edmunds Optics USB 3.0 CMOS camera, with a 480 × 752 pixel field of view and 8 bits. All images were captured with a Nikon ×20 objective (numerical aperture = 0.45) using bright-field microscopy, unless otherwise stated.

Computational model

A colloid is composed of a central core of diameter σ, interacting with other cores via an attractive (20 $k_B T$) cosine-squared potential of range 1.15σ and a repulsive Weeks–Chandler–Anderson potential for distances < σ. The surface of each core is decorated with 5 rigid patches, as in ref. 48, which interact with other patches with a weakly repulsive (10 $k_B T$) cosine-squared potential of diameter 0.15σ, thereby producing friction and transmitting rotation. Molecular dynamics simulations are performed using a Langevin thermostat with a characteristic time of ten time steps, so that motion is practically Brownian when no internal torque is applied. Simulations are performed in LAMMPS[49] and visualized with OVITO[50]. Details in the Supplementary Information.

Reporting summary

Further information on the research design is available in the Nature Portfolio Reporting Summary linked to this article.

Data availability

The data that support the plots within this paper and other findings of this study are available from the corresponding author upon request.

Code availability

The code that supports the plots within this paper and other findings of this study are available from the corresponding author upon request.

References

47. Oversteegen, S. & Lekkerkerker, H. On the accuracy of the Derjaguin approximation for depletion potentials. *Physica A: Stat. Mech. Appl.* **341**, 23–39 (2004).
48. Palaia, I. & Šarić, A. Controlling cluster size in 2D phase-separating binary mixtures with specific interactions. *J. Chem. Phys.* **156**, 194902 (2022).
49. Thompson, A. P. et al. LAMMPS—a flexible simulation tool for particle-based materials modeling at the atomic, meso, and continuum scales. *Comput. Phys. Commun.* **271**, 108171 (2022).
50. Stukowski, A. Visualization and analysis of atomistic simulation data with OVITO—the Open Visualization Tool. *Modell. Simul. Mater. Sci. Eng.* **18**, 015012 (2010).

Acknowledgements

D.G. and J.P. thank E. Krasnopeeva, C. Guet, G. Guessous and T. Hwa for providing the *E. coli* strains. This material is based upon work supported by the US Department of Energy under award DE-SC0019769. I.P. acknowledges funding by the European Union's Horizon 2020 research and innovation programme under Marie Skłodowska-Curie Grant Agreement No. 101034413. A.Š. acknowledges funding from the European Research Council under the European Union's Horizon 2020 research and innovation programme (Grant No. 802960). M.C.U. acknowledges funding from the European Union's Horizon 2020 research and innovation programme under Marie Skłodowska-Curie Grant Agreement No. 754411.

Author contributions

D.G. and J.P. conceived of the work and designed the experiment. D.G. performed the experimental research and analysed experimental data. I.P., A.Š., D.G. and J.P. designed the simulations. I.P. performed the simulations and analysed the data from the simulations. D.G., M.C.U., J.P. and E.H. performed the analytical modelling and related comparisons with experiments. D.G. and J.P. wrote the paper. D.G., I.P. and M.C.U. wrote the Supplementary Information. All authors reviewed and commented on the paper and on the Supplementary Information.

Competing interests

The authors declare no competing interests.

Additional information

Supplementary information The online version contains supplementary material available at https://doi.org/10.1038/s41567-023-02136-x.

Correspondence and requests for materials should be addressed to Jérémie Palacci.

Peer review information *Nature Physics* thanks Sofia Magkiriadou and the other, anonymous, reviewer(s) for their contribution to the peer review of this work.

nature portfolio

Corresponding author(s): Jeremie Palacci

Last updated by author(s): Jun 5, 2023

Reporting Summary

Nature Portfolio wishes to improve the reproducibility of the work that we publish. This form provides structure for consistency and transparency in reporting. For further information on Nature Portfolio policies, see our Editorial Policies and the Editorial Policy Checklist.

Statistics

For all statistical analyses, confirm that the following items are present in the figure legend, table legend, main text, or Methods section.

n/a	Confirmed	
☐	☒	The exact sample size (*n*) for each experimental group/condition, given as a discrete number and unit of measurement
☐	☒	A statement on whether measurements were taken from distinct samples or whether the same sample was measured repeatedly
☒	☐	The statistical test(s) used AND whether they are one- or two-sided *Only common tests should be described solely by name; describe more complex techniques in the Methods section.*
☒	☐	A description of all covariates tested
☒	☐	A description of any assumptions or corrections, such as tests of normality and adjustment for multiple comparisons
☐	☒	A full description of the statistical parameters including central tendency (e.g. means) or other basic estimates (e.g. regression coefficient) AND variation (e.g. standard deviation) or associated estimates of uncertainty (e.g. confidence intervals)
☒	☐	For null hypothesis testing, the test statistic (e.g. *F*, *t*, *r*) with confidence intervals, effect sizes, degrees of freedom and *P* value noted *Give P values as exact values whenever suitable.*
☒	☐	For Bayesian analysis, information on the choice of priors and Markov chain Monte Carlo settings
☒	☐	For hierarchical and complex designs, identification of the appropriate level for tests and full reporting of outcomes
☒	☐	Estimates of effect sizes (e.g. Cohen's *d*, Pearson's *r*), indicating how they were calculated

Our web collection on statistics for biologists contains articles on many of the points above.

Software and code

Policy information about availability of computer code

Data collection	The data collection that support the plots within this paper are described in the Supplementary Information
Data analysis	The code that support the plots within this paper and other findings of this study are available from the corresponding authors upon request.

For manuscripts utilizing custom algorithms or software that are central to the research but not yet described in published literature, software must be made available to editors and reviewers. We strongly encourage code deposition in a community repository (e.g. GitHub). See the Nature Portfolio guidelines for submitting code & software for further information.

Data

Policy information about availability of data

All manuscripts must include a data availability statement. This statement should provide the following information, where applicable:

- Accession codes, unique identifiers, or web links for publicly available datasets
- A description of any restrictions on data availability
- For clinical datasets or third party data, please ensure that the statement adheres to our policy

The data that support the plots within this paper and other findings of this study are available from the corresponding authors upon request.

Research involving human participants, their data, or biological material

Policy information about studies with human participants or human data. See also policy information about sex, gender (identity/presentation), and sexual orientation and race, ethnicity and racism.

Reporting on sex and gender	NA
Reporting on race, ethnicity, or other socially relevant groupings	NA
Population characteristics	NA
Recruitment	NA
Ethics oversight	NA

Note that full information on the approval of the study protocol must also be provided in the manuscript.

Field-specific reporting

Please select the one below that is the best fit for your research. If you are not sure, read the appropriate sections before making your selection.

☐ Life sciences ☐ Behavioural & social sciences ☐ Ecological, evolutionary & environmental sciences

For a reference copy of the document with all sections, see nature.com/documents/nr-reporting-summary-flat.pdf

Life sciences study design

All studies must disclose on these points even when the disclosure is negative.

Sample size	*Describe how sample size was determined, detailing any statistical methods used to predetermine sample size OR if no sample-size calculation was performed, describe how sample sizes were chosen and provide a rationale for why these sample sizes are sufficient.*
Data exclusions	*Describe any data exclusions. If no data were excluded from the analyses, state so OR if data were excluded, describe the exclusions and the rationale behind them, indicating whether exclusion criteria were pre-established.*
Replication	*Describe the measures taken to verify the reproducibility of the experimental findings. If all attempts at replication were successful, confirm this OR if there are any findings that were not replicated or cannot be reproduced, note this and describe why.*
Randomization	*Describe how samples/organisms/participants were allocated into experimental groups. If allocation was not random, describe how covariates were controlled OR if this is not relevant to your study, explain why.*
Blinding	*Describe whether the investigators were blinded to group allocation during data collection and/or analysis. If blinding was not possible, describe why OR explain why blinding was not relevant to your study.*

Behavioural & social sciences study design

All studies must disclose on these points even when the disclosure is negative.

Study description	*Briefly describe the study type including whether data are quantitative, qualitative, or mixed-methods (e.g. qualitative cross-sectional, quantitative experimental, mixed-methods case study).*
Research sample	*State the research sample (e.g. Harvard university undergraduates, villagers in rural India) and provide relevant demographic information (e.g. age, sex) and indicate whether the sample is representative. Provide a rationale for the study sample chosen. For studies involving existing datasets, please describe the dataset and source.*
Sampling strategy	*Describe the sampling procedure (e.g. random, snowball, stratified, convenience). Describe the statistical methods that were used to predetermine sample size OR if no sample-size calculation was performed, describe how sample sizes were chosen and provide a rationale for why these sample sizes are sufficient. For qualitative data, please indicate whether data saturation was considered, and what criteria were used to decide that no further sampling was needed.*
Data collection	*Provide details about the data collection procedure, including the instruments or devices used to record the data (e.g. pen and paper, computer, eye tracker, video or audio equipment) whether anyone was present besides the participant(s) and the researcher, and whether the researcher was blind to experimental condition and/or the study hypothesis during data collection.*
Timing	*Indicate the start and stop dates of data collection. If there is a gap between collection periods, state the dates for each sample cohort.*

Data exclusions	*If no data were excluded from the analyses, state so OR if data were excluded, provide the exact number of exclusions and the rationale behind them, indicating whether exclusion criteria were pre-established.*
Non-participation	*State how many participants dropped out/declined participation and the reason(s) given OR provide response rate OR state that no participants dropped out/declined participation.*
Randomization	*If participants were not allocated into experimental groups, state so OR describe how participants were allocated to groups, and if allocation was not random, describe how covariates were controlled.*

Ecological, evolutionary & environmental sciences study design

All studies must disclose on these points even when the disclosure is negative.

Study description	*Briefly describe the study. For quantitative data include treatment factors and interactions, design structure (e.g. factorial, nested, hierarchical), nature and number of experimental units and replicates.*
Research sample	*Describe the research sample (e.g. a group of tagged Passer domesticus, all Stenocereus thurberi within Organ Pipe Cactus National Monument), and provide a rationale for the sample choice. When relevant, describe the organism taxa, source, sex, age range and any manipulations. State what population the sample is meant to represent when applicable. For studies involving existing datasets, describe the data and its source.*
Sampling strategy	*Note the sampling procedure. Describe the statistical methods that were used to predetermine sample size OR if no sample-size calculation was performed, describe how sample sizes were chosen and provide a rationale for why these sample sizes are sufficient.*
Data collection	*Describe the data collection procedure, including who recorded the data and how.*
Timing and spatial scale	*Indicate the start and stop dates of data collection, noting the frequency and periodicity of sampling and providing a rationale for these choices. If there is a gap between collection periods, state the dates for each sample cohort. Specify the spatial scale from which the data are taken*
Data exclusions	*If no data were excluded from the analyses, state so OR if data were excluded, describe the exclusions and the rationale behind them, indicating whether exclusion criteria were pre-established.*
Reproducibility	*Describe the measures taken to verify the reproducibility of experimental findings. For each experiment, note whether any attempts to repeat the experiment failed OR state that all attempts to repeat the experiment were successful.*
Randomization	*Describe how samples/organisms/participants were allocated into groups. If allocation was not random, describe how covariates were controlled. If this is not relevant to your study, explain why.*
Blinding	*Describe the extent of blinding used during data acquisition and analysis. If blinding was not possible, describe why OR explain why blinding was not relevant to your study.*

Did the study involve field work? ☐ Yes ☒ No

Reporting for specific materials, systems and methods

We require information from authors about some types of materials, experimental systems and methods used in many studies. Here, indicate whether each material, system or method listed is relevant to your study. If you are not sure if a list item applies to your research, read the appropriate section before selecting a response.

Materials & experimental systems

n/a	Involved in the study
☒	☐ Antibodies
☒	☐ Eukaryotic cell lines
☒	☐ Palaeontology and archaeology
☒	☐ Animals and other organisms
☒	☐ Clinical data
☒	☐ Dual use research of concern
☒	☐ Plants

Methods

n/a	Involved in the study
☒	☐ ChIP-seq
☒	☐ Flow cytometry
☒	☐ MRI-based neuroimaging